optica

Pupil function engineering for enhanced nanoparticle visibility in wide-field interferometric microscopy

Oguzhan Avci,[1] Maria I. Campana,[1] Celalettin Yurdakul,[1] and M. Selim Ünlü[1,2,*]

[1]Department of Electrical and Computer Engineering, Boston University, Boston, Massachusetts 02215, USA
[2]Department of Biomedical Engineering, Boston University, Boston, Massachusetts 02215, USA
*Corresponding author: selim@bu.edu

Received 6 December 2016; revised 16 January 2017; accepted 19 January 2017 (Doc. ID 281965); published 14 February 2017

Wide-field interferometric microscopy techniques have demonstrated their utility in sensing minute changes in the optical path length as well as visualization of sub-diffraction-limited nanoparticles. In this work, we demonstrate enhanced signal levels for nanoparticle detection by pupil function engineering in wide-field common-path interferometric microscopy. We quantify the improvements in nanoparticle signal achieved by novel optical filtering schemes, benchmark them against theory, and provide physical explanations for the signal enhancements. Our refined common-path interferometric microscopy technique provides an overall ten-fold enhancement in the visibility of low-index, non-resonant polystyrene nanospheres ($r \sim 25$ nm), resulting in nearly 8% signal-to-background ratio. Our method can be a highly sensitive, low-cost, label-free, high-throughput platform for accurate detection and characterization of weakly scattering low-index nanoparticles with sizes ranging from several hundred down to a few tens of nanometers, covering nearly the entire size spectrum of biological particles.

OCIS codes: (180.3170) Interference microscopy; (070.0070) Fourier optics and signal processing; (220.1230) Apodization.

https://doi.org/10.1364/OPTICA.4.000247

1. INTRODUCTION

Scientists have been fascinated with visualizing the microscopic world for hundreds of years [1,2]. Conventional optical microscopy based on light scattering cannot detect features that are significantly smaller than the wavelength of illumination. The diffraction barrier in optical resolution can be surpassed in fluorescence microscopy [3]. With the advent of non-optical microscopes, it has become possible to visualize the nanoscale biological particles. We now know that synthetic and natural nanoparticles—generally defined as having a size of 10–100 nm—have enormous utility in biotechnology and medicine as well as potential adverse impact on human health and food safety [4–6]. Perhaps the most abundant nanoparticles are viruses, with an estimated $\sim 10^{32}$ phages in the biosphere [7] and $\sim 10^{7}$ viruses on average in a milliliter of seawater [8]. The viruses vary from ~20 nm to hundreds of nanometers in diameter [9,10]. Another class of abundant biological nanoparticles is exosomes, phospholipid nanovesicles which are secreted by mammalian cells [11]. The interest in these vesicles has grown exponentially over the last several years following the discovery that they are involved in intercellular communication by serving as transfer vehicles of proteins, mRNA, and miRNA between cells [12]. Their sizes range from 30 to 100 nm [13]. Optical detection and visualization of biological nanoparticles represents unique challenges and opportunities due to small particle size and low refractive index contrast. Among optical techniques, elastic-light-scattering-based detection methods (direct detection without labels) are more robust than fluorescence methods owing to the signal stability. However, since the elastically scattered light intensity induced by the illumination of the nanoparticles scales with the square of polarizability, it is very challenging to detect small, low-index biological nanoparticles over the background reflections. To overcome this difficulty, nanoparticle sensing through interferometry has been realized with the prominent advantage in sensitivity over other optical techniques in which signals are based solely on scattered light intensity [14–16]. Furthermore, interferometry has also been extensively used as a powerful technique that is highly susceptible to infinitesimal changes in optical path/media, allowing for extremely sensitive measurements in various fields such as biosensing, astronomy, and range detection [17–19].

The significant sensitivity advantage in interferometric nanoparticle detection stems from the fact that the particle signal consists of the cross (interference) term that scales with particle polarizability and hence particle volume [20]. In contrast, the nanoparticle signal in the scattering-based non-interferometric imaging scales with the square of polarizability, which leads to a rapid falloff in the signal, rendering the smaller-scale nanoparticles indistinguishable from the background. The interferometric signal, however, provides superior sensitivity by scaling linearly with particle volume. Utilizing the interferometric enhancement

phenomenon, we previously developed a wide-field imaging technique, single-particle interferometric reflectance imaging sensor (SP-IRIS) that is capable of detecting individual low-index, non-resonant nanoparticles down to 70 nm in diameter [16], allowing for direct characterization of particles simultaneously and in a multiplexed fashion.

Pupil function engineering has been employed extensively in optical techniques ranging from super-resolution microscopy to lithography [21–25]. Particularly, it allows for optimization of an optical system for a particular application, whether it be light confinement or extension of the resolving power of an imaging system in axial and lateral dimensions. In this work, we realize pupil function engineering in a wide-field interferometric imaging scheme to improve on its nanoparticle detection sensitivity. We introduce pupil function engineering into the current system in two steps: first we use a mask in the illumination path to control the NA of the illumination, i.e., the angular content of excitation light, for efficient collection of the enhanced scattering of nanoparticles in the vicinity of the layered sensor surface. The second step uses a custom-made spatial reflective transmission filter in the Fourier plane of the collection path for background signal reduction. Moreover, a rigorous physical model for the interference-enhanced nanoparticle imaging [20] has been utilized as a forward model in this study. Our refined optical imaging method has the potential to be a highly sensitive, low-cost, label-free, high-throughput detection platform to study weakly scattering, low-index biological nanoparticles, such as viruses [26,27] and exosomes [28], with sizes ranging from several hundred down to a few tens of nanometers, covering nearly the entire range of biological nanoparticles.

2. SINGLE-PARTICLE INTERFEROMETRIC REFLECTANCE IMAGING SENSOR

The SP-IRIS uses a layered sensor composed of a thin layer of glass (typically SiO_2) atop a Si substrate in a common-path interferometry configuration. The signal is based on interference between the scattered field from the particle of interest and the reference field reflected off the sensor, thus allowing for higher sensitivity levels owing to volume dependence of the signal. We also achieve enhanced scattering of nanoparticles in the collection direction given the tuned thickness of the glass layer, similar to engineering a dipole antenna directivity [29]. The SP-IRIS signal is also affected by the polarizability of the particle, amplitude of the reference field, and the phase lag between them as discussed in more detail in the next section.

3. THEORY

The SP-IRIS technique employs a Köhler illumination scheme with a low-coherence light source that is typically a light-emitting diode. Köhler illumination enables source-free imaging of the sample by mapping the Fourier plane of the light source to the sample plane. In this configuration, the light source and the back focal aperture of the objective (A_{bf}) are conjugate planes with respect to one another. Each point in the light source produces a plane wave—that is incoherent with regard to others—incident on the sample at an angle defined by its position in the transverse plane. Therefore, control over illumination NA (illumination angles) can be achieved by placing a mask (A_{il}) in front of the light source as depicted in Fig. 1. Furthermore, the incoherent

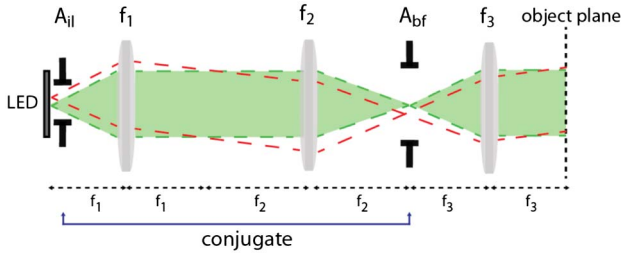

Fig. 1. Köhler illumination geometry with integrated mask (A_{il}) for angular control over excitation light. (Adapted from [20].)

nature of these plane waves with respect to each other can be explained by the lack of fixed phase relationships among them owing to the spatial incoherence of the light source. We can formulate the total driving field component ($\mathbf{E}_{t,m}$) due to a point in the plane of the light source (defined by the mask in the illumination) as follows:

$$\mathbf{E}_{t,m} = \overleftrightarrow{\mathbf{H}}_{t,m}\mathbf{E}_{i,m}, \tag{1}$$

where $\overleftrightarrow{\mathbf{H}}_{t,m} = \overleftrightarrow{\mathbf{H}}_{i,m} + \overleftrightarrow{\mathbf{H}}_{r,m}$ denotes the transfer functions defined by illumination geometry ($\overleftrightarrow{\mathbf{H}}_{i,m}$) and reflections from the layered substrate ($\overleftrightarrow{\mathbf{H}}_{r,m}$). Each incident light component ($\mathbf{E}_{i,m}$) interacts with the sample separately, resulting in a scattered electric field and specularly reflected reference field, which later interfere in the detector plane. As the particle sizes of interest are much less than the wavelength of the illuminating light, the dipole approximation for the scattered field calculations holds true [30]. Hence, the scattered field components can be defined assuming a point dipole scatterer. Using the angular spectrum representation (ASR) of Green's functions [30] that constitute both the primary ($\overleftrightarrow{\mathbf{G}}_{o,m}$) and reflected ($\overleftrightarrow{\mathbf{G}}_{r,m}$) field components defined by the geometry of the optical system, as well as the layered sensor, we can formulate the scattered field components in the image plane as follows:

$$\mathbf{E}^{u}_{s,m} = \frac{k_o^2}{\epsilon_o}\overleftrightarrow{\mathbf{G}}_{s,m}\mathbf{p}, \tag{2}$$

where

$$\overleftrightarrow{\mathbf{G}}_{s,m} = \overleftrightarrow{\mathbf{G}}_{o,m} + \overleftrightarrow{\mathbf{G}}_{r,m}, \tag{3}$$

$$\mathbf{p} = \epsilon_m \alpha \mathbf{E}_{t,m}, \tag{4}$$

$$\alpha = 4\pi r^3 \frac{\epsilon_p - \epsilon_m}{\epsilon_p + 2\epsilon_m}. \tag{5}$$

$\mathbf{p}$ denotes the dipole moment, the u superscript denotes fields in the image plane, α denotes the particle polarizability, k_o denotes the wavenumber, and ϵ_p and ϵ_m denote the permittivities of particle and surrounding medium, respectively. Similar to the treatment of mapping of incident field components to the sample plane using the ASR model, we can map the reflected reference field to the image plane as follows:

$$\mathbf{E}^{u}_{r,m} = \overleftrightarrow{\mathbf{H}}_{r,m}\mathbf{E}_{i,m}, \tag{6}$$

where $\overleftrightarrow{\mathbf{H}}_{r,m}$ denotes the transfer function defined by both the illumination and imaging optics. Finally, we incoherently sum the intensities calculated with the reflected and scattered fields within

the angular spectrum range to find the full intensity response of the system for a given particle:

$$I_t = \sum_{m\epsilon \mathrm{NA}} |\mathbf{E}^u_{r,m} + \mathbf{E}^u_{s,m}|^2. \quad (7)$$

In other words, each intensity recording is added to the final image incoherently—where the final image is the sum of all the intensity recordings corresponding to the plane waves within the NA of the optical system. The reader is referred to [20] for a more detailed discussion on the physical model.

4. ENGINEERING THE LIGHT SCATTERING FROM SUB-WAVELENGTH NANOPARTICLES USING LAYERED MEDIA

As previously mentioned, nanoparticles that are much smaller than the excitation wavelength can be approximated as dipole scatterers. Moreover, in the vicinity of planar interfaces, they can scatter light in a certain direction with respect to the incident light angle. We engineer this to enhance the scattering in the direction of light collection for a given wavelength. For example, in reflected light microscopy that uses a narrowband green light source (with $\lambda_o = 525$ nm), scattering enhancement from a nanoparticle in the collection (backward) direction can be achieved by designing a layered sensor surface that allows for constructive interference between the backward scattered light and the reflection of forward scattered light. This constructive self-interference of the scattered fields is a function of the layer thickness (d) and wavelength of illuminating light, and the layered media can be constructed according to the illumination wavelength to maximize it (i.e., $d \sim \lambda_2/4$, where $\lambda_2 = \lambda_o/n_2$). Notice that this enhancement by self-interference cannot be achieved using a broadband light source, as the layer thickness will only allow constructive interference for a narrow range of wavelengths. We illustrate this overall light enhancement from a nanoparticle in Fig. 2(b) for the green light. Note that the simulations use a single wavelength for the sake of simplicity, which also provides a reasonable approximation for narrow-bandwidth light sources provided that their coherence length is greater than the thickness of the layer, d. This is easily achieved with LEDs that typically exhibit several-micrometer coherence length, since d is of the order of hundreds of nanometers. On the other hand, lasers can exhibit extremely long coherence lengths of the order of meters; however, their use as illumination sources in such wide-field imaging systems is limited due to speckle in the images owing to the highly coherent nature of these light sources. There are ways of reducing the speckle in laser imaging systems at the expense of additional bulky optical components, as investigated in [31].

The simple idea of engineering a layered substrate to increase the collected scattered light from nanoparticles constitutes the foundation of interference-enhanced nanoparticle imaging with SP-IRIS. The choice of material for the layered substrate is SiO_2/Si, as thermal oxidation on Si is a controlled and well-optimized process in microfabrication that ensures optical quality surfaces that are broadly compatible with bioassay applications as discussed in [31].

So far, we have only assumed a dipole orientation in the horizontal direction. However, for high-NA illumination geometries, a considerable amount of dipole excitation occurs in the vertical direction, i.e., vertical dipole excitation increases with increasing angle of incidence (θ). Therefore, it is imperative to investigate the radiation patterns for the vertically oriented dipole with the same layered sensor design. Since there is no radiation along the dipole orientation, the radiation pattern for a vertically aligned dipole is mostly at high angles that are typically not within the range of collection optics, as shown in Fig. 3(b). Furthermore, the optimized layered substrate for a horizontal dipole ($d = 100$ nm case) has diminishing returns for the vertically oriented dipole, as can be seen in Fig. 3(b). Note that we limit our discussion on the dipole radiation patterns to the case in which the dipole is resting on the surface, which is a valid assumption for smaller-scale nanoparticles ($r < 50$ nm) as their center is quite close to the surface. The radiation patterns will vary from those in Figs. 2(b) and 3(b) when the dipole is elevated from the surface owing to the additional phase introduced by the elevation, which is the case with larger-scale nanoparticles as can be seen in Supplement 1. However, the signal enhancement via pupil function engineering is of particular importance for the smaller-scale nanoparticles, as larger ones already exhibit appreciable signal levels without any pupil function engineering due to their large scattering cross-sections (see Fig. S1).

Though it is outside the scope of this study, it is worth noting that further increasing d, the thickness of the layer with n_2 refractive index, would result in higher-order radiation patterns. Therefore, angular confinement can be achieved for the scattered field by adjusting the thickness of the layered sensor, providing means

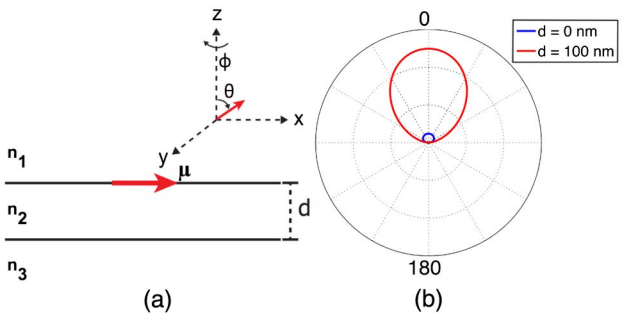

Fig. 2. Layered sensor design can be utilized to enhance the horizontally aligned dipole scattering in direction of collection. (a) Layered sensor design for common-path interferometry; (b) normalized dipole radiation patterns in the plane of dipole axis and z axis for $n_1 = 1$, $n_2 = 1.45$, and $n_3 = 4$ when $d = 0$ nm and $d = 100$ nm. Note that the excitation wavelength is chosen to be 525 nm.

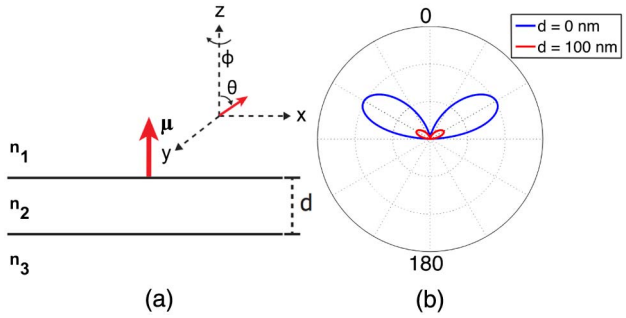

Fig. 3. Vertically oriented dipole atop a layered sensor and its scattering in the direction of collection. (a) Layered sensor design for common-path interferometry; (b) normalized dipole radiation patterns in the plane of dipole axis and z axis for $n_1 = 1$, $n_2 = 1.45$, and $n_3 = 4$ when $d = 0$ nm and $d = 100$ nm. Note that the excitation wavelength is chosen to be 525 nm.

to spatially separate it from the reference field in the Fourier plane of the collection path. This can potentially allow for more controlled implementations of pupil function engineering as well as for optical scatter imaging [32] type measurements. In such an experimental design, the coherence length of the light source is the limiting factor for the thickness (d).

5. INTERFEROMETRIC SIGNAL ENHANCEMENT

Suppose two coherent plane waves, $\mathbf{E}_1 = A_1 e^{i\phi_1}$ and $\mathbf{E}_2 = A_2 e^{i\phi_2}$, interfere on a detector plane. The recorded intensity can be formulated as follows:

$$I_t = |\mathbf{E}_1 + \mathbf{E}_2|^2 = A_1^2 + A_2^2 + 2A_1A_2\cos(\phi_1 - \phi_2), \quad (8)$$

where A_1 and A_2 represent the real-valued amplitude, and ϕ_1 and ϕ_2 represent the phase for E_1 and E_2, respectively. Notice that the recorded intensity is maximized when the two waves are in phase, i.e., $\phi_1 - \phi_2 = m \times 2\pi$ where m is an integer. Furthermore, if we consider E_1 as the reference field and E_2 as the scattered field as in Eq. (7), the signal-to-background ratio obtained from the nanoparticle, also known as the normalized intensity ($I_{\text{norm}} = I_t/I_r$ where $I_r = |E_1|^2$), can be written as follows:

$$I_{\text{norm}} = 1 + \frac{A_2^2}{A_1^2} + 2\frac{A_2}{A_1}\cos(\phi_1 - \phi_2). \quad (9)$$

Note that assuming the amplitudes of these fields, A_1 and A_2, are independent from one another, the normalized intensity has no upper bound, i.e.,

$$\lim_{A_1 \to 0} I_{\text{norm}} \to \infty \quad (10)$$

given that the signal is above the noise floor, which follows the Poisson statistics for a shot-noise limited detection system. Therefore, in principle, reducing the amplitude of the reference field could increase the normalized intensity for a nanoparticle significantly—assuming the collected signal stays above the noise floor. In practice, however, detector integration time, number of frames averaged, and stray light from back reflections are the main factors that limit the nanoparticle signal.

6. PUPIL FUNCTION ENGINEERING SCHEMES IN WIDE-FIELD INTERFEROMETRIC MICROSCOPY FOR ENHANCED NANOPARTICLE SIGNAL

In light of our theory-based observations, we investigate methods for optimizing the interferometric nanoparticle signal in terms of the angular content of the illumination light as well as the amplitudes of the signal constituents, i.e., the reference and scattered fields. First, we examine the optimal interferometric nanoparticle excitation in terms of illumination NA given the angular limit in the light collection set by the NA of the objective. Second, we will focus on reducing the amplitude of the background light to further enhance the nanoparticle signal.

A. Experimental Setup

The digital detection of nanoscale particles requires imaging with high resolution and sufficient spatial sampling. Therefore, our technique uses an objective with high magnification and high NA as well as an imager that is typically a CCD camera with a sufficiently small pixel pitch, ensuring the Nyquist sampling criterion that is the desired spatial sampling rate is at least twice the resolution [33] as follows:

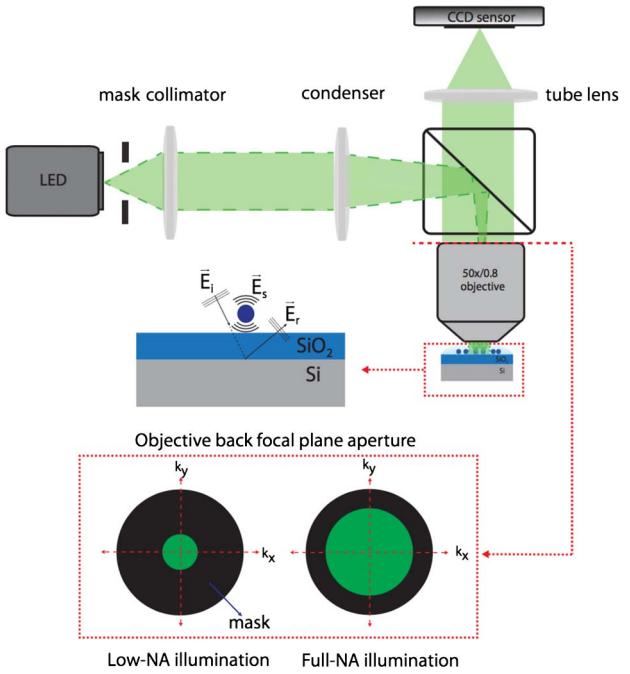

Fig. 4. Wide-field interferometric microscopy setup. The mask in the illumination path controls the illumination NA, allowing for signal optimization.

$$\begin{aligned}\text{Spatial sampling rate} &= \text{Effective pixel size}\\ &= \text{Pixel pitch}/\text{Magnification}\\ &\le \text{Resolution}/2 \approx \lambda/(4\ \text{NA}).\end{aligned} \quad (11)$$

As depicted in Fig. 1, the illumination path of the experimental setup consists of a low-coherent light source (an LED), an amplitude transmission mask placed in front of the active region of the LED, and a two-lens system, which images the mask onto the back focal aperture of the objective. The mask diameter can be manually adjusted to control the NA of illumination. For the first part of the study, we use a high-NA objective and a tube lens in the collection path of the setup, forming a two-lens imaging system, and image the object plane onto a CCD camera as shown in Fig. 4. For the second part, we add a 4f system in the collection path to relay the back focal plane of the objective to the filter plane and image this plane with a tube lens as shown in Fig. 6(a). In both experiments, we use a 50 × /0.8 NA objective (Nikon Inc.), 12 megapixel CCD camera (GS3-U3-120S6M-C, Point Grey Research Inc.), and a layered sensor that is composed of a 100 nm SiO_2 layer atop a single side polished Si substrate. The sample is prepared by spin-coating the layered sensor surface with 25 nm nominal-radius polystyrene nanoparticles (Phosphorex Inc.).

B. Pupil Function Engineering in the Illumination Path

In this section, we investigate the effects of illumination NA on the visibility of spherical nanoparticles. The motivation to engineer the illumination NA stems from the orientation of the dipole moment excitation as a function of the incidence angle (θ) of the illuminating light. As the incidence angle increases, the dipole excitation in the vertical direction increases and, as a result, energy is radiated at degrees outside the collection range of the objective [as shown in Fig. 3(b)], which is 0°–53° for a 0.8 NA objective lens.

However, since SP-IRIS uses epi-illumination, those high-angle illumination rays end up getting specularly reflected from sensor surface and collected by the objective. As a result, their contribution to the background signal dominates the resultant scattered light that is both unenhanced and poorly collected. Therefore, limiting the illumination to a lower NA ensures excitation of dipoles mostly in the horizontal direction, which, in conjunction with the layered sensor design, have an enhanced radiation pattern well within the range of collection angles as shown in Fig. 2(b). Moreover, while the layered media design with $d \sim \lambda_2/4$ enhances the scattered fields, it also reduces the background signal by destructive interference for low-NA illumination. In light of these observations, we conducted an optimization study using the physical model detailed in Section 3. The parameter we sweep in this study is the range of illumination NAs for a setup that uses 50 × /0.8 NA objective and a 25 nm radius polystyrene nanosphere atop a SiO_2/Si layered sensor with 100 nm oxide layer, as shown in Fig. 4.

The nanoparticle response is simulated for illumination NAs ranging from 0.05 to 0.8. For instance, when the illumination NA is 0.3, the simulation considers an illumination scheme that spans incident plane waves from 0° to 17°. As can be seen in Fig. 5(a), the maximum normalized intensity obtained from a polystyrene nanosphere increases with decreasing illumination NA, converging to a 2.5% signal at the lower end of the parameter boundary.

It is important to note that in the full-NA illumination case, which is what the conventional SP-IRIS uses, the signal of a 25 nm radius polystyrene nanosphere is much less than 1%, the empirically considered limit of detection, hence undetectable. This limit of detection is determined based on the background signal fluctuations due to morphological variations in antibody spots that are typically used for biological nanoparticle capture [34]. As a result of this optimization study on the illumination, low-index, non-resonant polystyrene nanoparticles with 25 nm nominal radius are expected to be rendered visible in SP-IRIS. To experimentally validate this, we have chosen two illumination configurations: (i) low-NA illumination where the illumination is limited to 0.3 NA, (ii) full-NA illumination where the illumination is set to 0.8 NA defined by the objective. Notice that as the cone of light incident on the nanoparticles gets smaller, i.e., illumination NA decreases, the exposure time necessary to operate in the shot-noise limited regime increases. Therefore, for the low-NA illumination case, instead of picking the NA that provides the highest signal, we trade that for a shorter exposure time and settle for 0.3 NA illumination. It is also physically less challenging to ensure 0.3 NA illumination than that of 0.05 NA in the paraxial regime. In return, the signal loss is quite negligible—less than 0.2%. In practice, one can employ multiple high-power LEDs in the system if short acquisition time is essential for the application. The theory suggests nearly a five-fold improvement in the normalized intensity percentage (from 0.5% to 2.3%) of

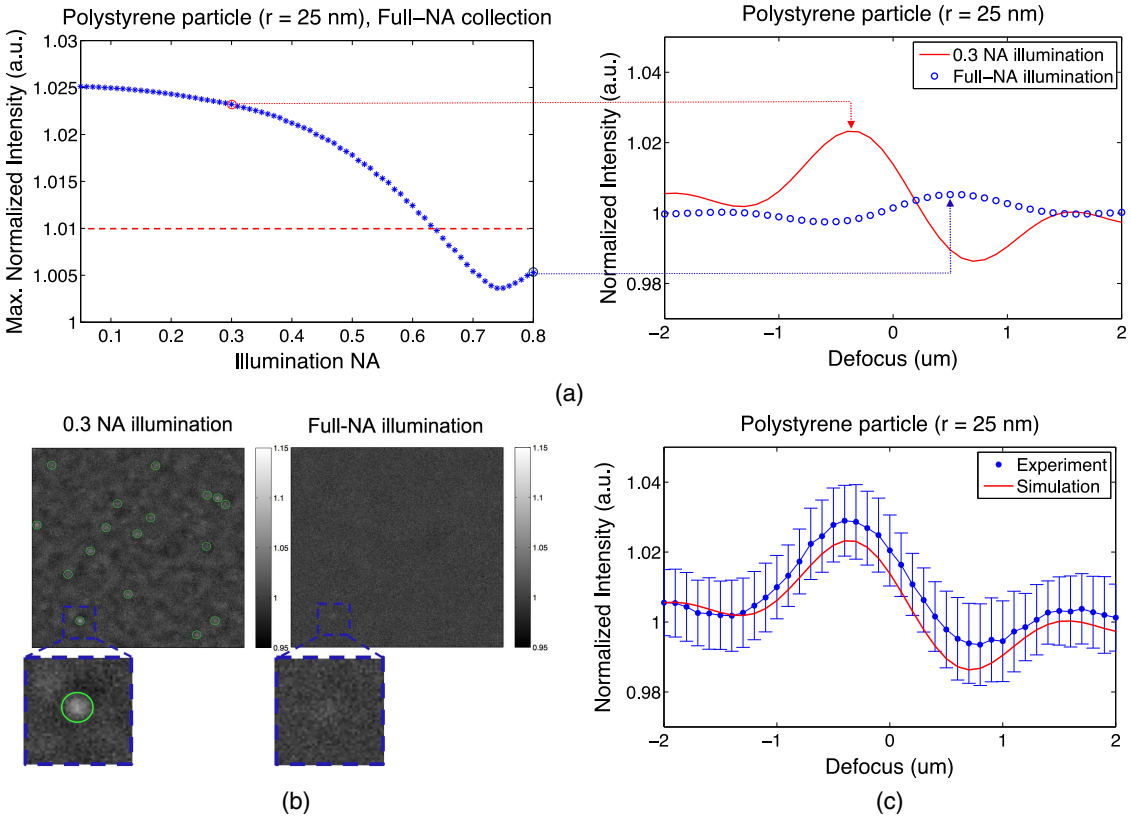

Fig. 5. (a) (Left) Maximum nanoparticle signal simulation with respect to illumination NA. For example, for a maximum illumination NA of 0.3, the sample gets illuminated by light rays spanning angles corresponding to 0° to 17°. The red dashed line around 1.01 indicates the limit of detection in terms of particle visibility, i.e., <1% normalized intensity is considered indistinguishable from the background fluctuations. (Right) Defocus scans of low-NA illumination (0.3 NA) and full-NA illumination (0.8 NA) cases. (b) Median normalized 25 nm radius polystyrene nanosphere images at their highest signal z plane for low- and full-NA configurations. (c) Experimentally obtained average defocus data benchmarked against the simulations. The experimental data points are laid on top of the red simulation curve from (a).

25 nm radius polystyrene signal as shown in the defocus curves for both cases in Fig. 5(a).

As discussed in our previously published work [20], the defocus is defined as the axial shift of the top sensor surface from the focal plane of the objective lens. It is of great importance to acquire and analyze defocus scans for this type of interferometric measurement, as maximized visibility (i.e., maximum signal-to-background ratio) for a nanoparticle can occur in different z planes depending on particle size and the NAs of the illumination and collection, attributed to the change in phase between the reflected reference field and scattered field components. The experimental data for the low-NA (0.3 NA) illumination case is obtained by averaging the responses of 189 detected polystyrene nanospheres with 25 nm nominal radius. As can be seen in Fig. 5(c), it demonstrates a great agreement with theory. The slight deviations in the experimental data from the theory can be ascribed to size variations of the nanospheres. The polystyrene nanospheres (circled in green) are clearly visible in SP-IRIS with low-NA illumination configuration as opposed to the full-NA configuration, as shown by the median normalized images of the same field of view in Fig. 5(b). Note that the images in Fig. 5(b) show the highest signal defocus plane nanoparticle responses for both configurations. As predicted by theory, in the full-NA illumination case, the polystyrene nanospheres are neither visible nor detectable by our custom MATLAB particle-detection software [Fig. 5(b)].

C. Pupil Function Engineering in the Collection Path

In addition to the pupil function engineering in the illumination path, Fourier filtering in the collection path can be carried out by relaying the back focal plane of the objective to a conjugate plane using a 4f system, as shown in Fig. 6(a). As previously mentioned, the aim in this case is to reduce the amplitude of the reference field components. This essentially allows for the excitation of nanoparticles with high-power illumination without saturating the detector with high background signal [see Eq. (10)]. This in turn can further enhance the interferometric signal, especially for weakly scattering nanoparticles, if the low-NA illumination is used and a spatial transmission filter in the Fourier plane of the collection arm covers the whole angular spectrum of the illumination rays, reducing their specularly reflected fields' amplitudes (i.e., reference field components). While all the reference field components experience this reduction, only a part of the scattered field components (low-angle scattered rays) will go through an amplitude reduction, allowing for a potential enhancement in the overall signal. In addition to the background signal reduction capability, our defocus scan data-acquisition scheme allows us to sweep the phase difference between the specularly reflected reference field components (mostly along the optic axis since low-NA illumination is employed) and the scattered field components (which cover the whole angular range set by objective NA) to sample the interference curve and achieve maximum signal-to-background ratio at a particular defocus point. In a way, our system enables partial control over both the phase and amplitude of the signal constituents of a common-path interferometer. To verify our hypothesis experimentally, we use a custom-made spatial reflective transmission filter with an optical density of 1.3 in a circular region with a diameter of 3.2 mm that corresponds to 0.4 NA of the angular spectrum of 0.8 NA collection. The filter consists of a gold layer patterned on a glass cover slip, and its empirically verified transmission profile is given in Fig. 6(b). The reference beam in the back pupil aperture of the objective,

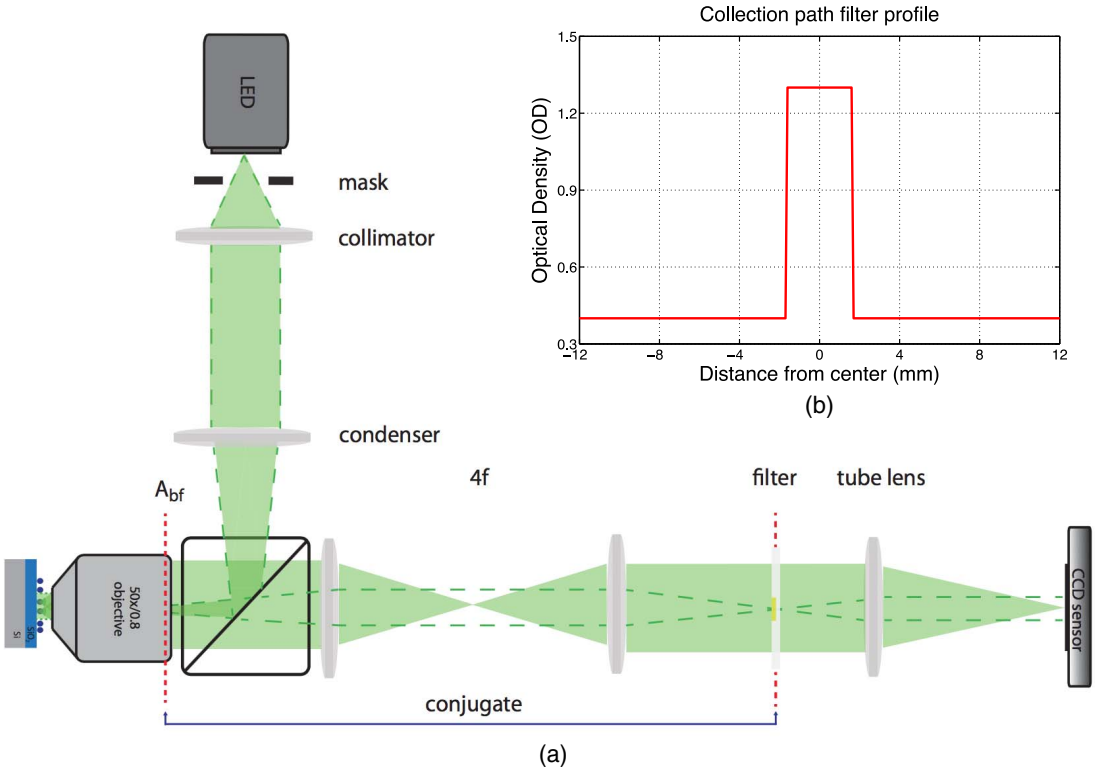

Fig. 6. (a) Wide-field interferometric microscopy setup demonstrating masks in both the illumination and collection paths. The 4f system in the collection path relays the back focal plane of the objective to a conjugate plane where the filter is placed. (b) Custom-made filter transmission profile.

and hence on the filter, is set to be 1.6 mm in diameter, corresponding to 0.2 NA illumination assuming paraxial approximation. In this case, 0.2 NA illumination ensures ease of alignment of the reference field with regards to 0.4 NA spatial filter, providing a sufficient power level of the illumination light for a reasonable exposure time in image acquisition. As can be seen from the filter profile in Fig. 6(b), the center of the filter (with radius of 1.6 mm) has a transmission rate of 0.05 and the transmission rate on the rest of the filter on glass is 0.4. In the Köhler illumination scheme, as the light source is imaged on the back focal plane of the objective and that same plane is relayed to the filter plane, we can effectively reduce the reference intensity by around 95%. The scattered field, on the other hand, is in the Fourier plane in the back focal aperture of the objective, hence also in the plane where the filter lies, and it encompasses a region of 6.4 mm in diameter on the filter. This area is essentially determined by the NA of the objective and the magnification of the 4f system. The high-spatial-frequency components of the scattered field (>0.4 NA) do not encounter this highly lossy part of the filter, enabling partial signal adjustment between the reference field and part of the scattered field. Therefore the scattered field, especially the higher-spatial-frequency components, encounters a transmission rate that is a lot higher than what the reference field encounters, allowing for the interferometric signal constituents to be more comparable to one another amplitude-wise. The experiments use 25 nm radius polystyrene nanospheres, as in the previous section. As can be seen in Fig. 7(a), where the highest signal defocus plane nanoparticle responses obtained with 1.3 OD spatial filter and no filter configurations are shown, considerable nanoparticle signal enhancement is achieved for low-index,

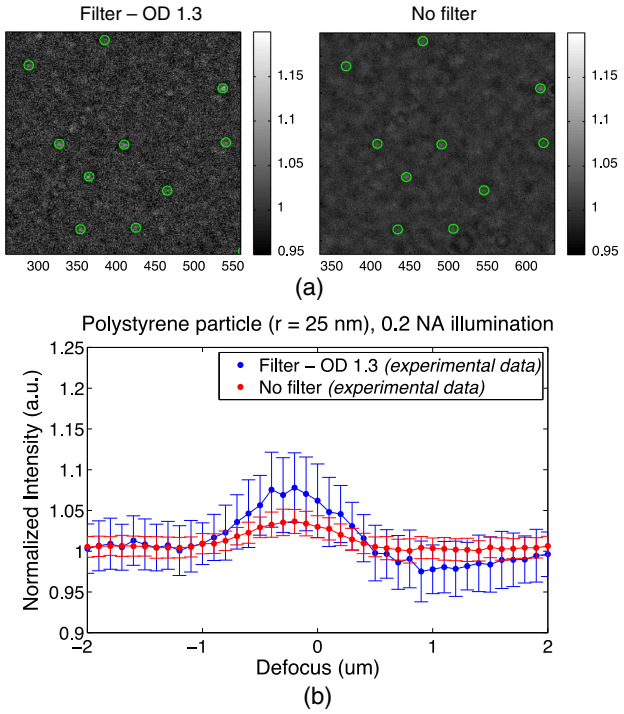

Fig. 7. Further nanoparticle signal enhancement through spatial filtering. (a) Median normalized 25 nm radius polystyrene nanosphere images at their highest signal z plane for 1.3 OD spatial filter and no filter configurations. (b) Experimentally obtained average defocus data of polystyrene nanospheres with 25 nm nominal radius.

non-resonant nanospheres with a nominal radius of 25 nm. The normalized intensity percentage, obtained by averaging the responses of 76 detected 25 nm nominal radius polystyrene particles, is enhanced by over a factor of 2—increasing from 3.7% to 7.8% [Fig. 7(b)]. The experimental data for the no-filter case (red dots) and 1.3 OD spatial filter case (blue dots) were obtained using custom MATLAB software that does particle registration across images for comparative analysis of particle responses in different conditions (e.g., filter case versus no filter case).

7. CONCLUSION

In this study, we have demonstrated the integration of pupil function engineering into a wide-field interferometric imaging scheme. By modifying both illumination and collection paths, a significant enhancement in single-nanoparticle detection is achieved. We have discussed the signal constituents in detail and the motivation to carry out Fourier filtering in both illumination and collection paths of the optical system. By implementing pupil modification in the illumination path, we have successfully shown the detection of low-index, non-resonant polystyrene nanospheres of 25 nm nominal radius with a more than 3% signal-to-background ratio in SP-IRIS, representing a five-fold signal improvement over conventional full-NA Köhler illumination. This enhancement in the nanoparticle signal can be attributed to the fact that the sub-wavelength nanoparticles scatter the incident light as electric dipoles, and, by studying the nature of the energy radiation from the electric dipole in the vicinity of a layered sensor surface, the radiation patterns can be engineered—much like the dipole antenna directivity. The interferometric nanoparticle signal then can be maximized with the optimized illumination geometry, making even the smaller-scale sub-wavelength nanoparticles visible in a wide-field imaging setting. Therefore, the conventional method of implementing full-NA illumination by filling the back focal aperture of the objective in Köhler illumination geometry does not provide the optimal nanoparticle signal in wide-field common-path interferometric imaging, owing to the inefficient collection of the scattered light. Optimal nanoparticle excitation and the resultant scattered light collection in the vicinity of a layered sensor surface are achieved in a low-NA illumination and full-NA collection configuration. In addition to the enhancement rendered by pupil function engineering in the illumination path, we also have shown that the interferometric nanoparticle signal can further be enhanced with the implementation of a spatial reflective transmission filter placed in the Fourier plane of the collection path. This filter approach enables us to reduce the amplitude of the reference field, making it more comparable to the amplitude of the weakly scattered field—which in turn results in an improved signal-to-background ratio. We report an additional two-fold increase in the normalized intensity contrast in the observed nanoparticle signal, resulting in a nearly 8% signal-to-background ratio for 25 nm radius polystyrene nanoparticles. In conclusion, compared to conventional SP-IRIS, our refined wide-field interferometric microscopy technique provides an overall ten-fold enhancement in nanoparticle signal, which can render particles of sizes below 50 nm in diameter visible in a multiplexed fashion. Given that the nanoparticle signal in an interferometric measurement scales with particle polarizability, and hence particle volume, we expect to be able to detect low-index nanoparticles down to 12 nm in radius with a conservative limit of detection at 1%. Therefore, our

method can be a promising high-throughput, label-free, and highly sensitive detection platform for studying weakly scattering biological particles such as viruses and exosomes, covering almost their full size ranges.

Funding. I/UCRC Center for Biophotonic Sensors and Systems (CBSS).

Acknowledgment. The authors thank Dr. Ronen Adato and Dr. Abdulkadir Yurt for their insightful discussions.

See Supplement 1 for supporting content.

REFERENCES

1. R. Hooke, *Micrographia: or, Some Physiological Descriptions of Minute Bodies Made by Magnifying Glasses* (J. Martyn and J. Allestry, 1665).
2. P. Fara, "A microscopic reality tale," Nature **459**, 642–644 (2009).
3. The Nobel Prize in Chemistry (Nobel Media, 2014), http://www.nobelprize.org/nobel_prizes/chemistry/laureates/2014/.
4. C. M. Somers, B. E. McCarry, F. Malek, and J. S. Quinn, "Reduction of particulate air pollution lowers the risk of heritable mutations in mice," Science **304**, 1008–1010 (2004).
5. M. V. Yezhelyev, X. Gao, Y. Xing, A. Al-Hajj, S. Nie, and R. M. O'Regan, "Emerging use of nanoparticles in diagnosis and treatment of breast cancer," Lancet Oncol. **7**, 657–667 (2006).
6. Y. Cao, J. Li, F. Liu, X. Li, Q. Jiang, S. Cheng, and Y. Gu, "Consideration of interaction between nanoparticles and food components for the safety assessment of nanoparticles following oral exposure: a review," Environ. Toxicol. Pharmacol. **46**, 206–210 (2016).
7. R. W. Hendrix, M. C. M. Smith, R. N. Burns, M. E. Ford, and G. F. Hatfull, "Evolutionary relationships among diverse bacteriophages and prophages: All the world's a phage," Proc. Natl. Acad. Sci. USA **96**, 2192–2197 (1999).
8. C. A. Suttle, "Viruses in the sea," Nature **437**, 356–361 (2005).
9. G. F. Brooks, K. C. Carroll, J. S. Butel, S. A. Morse, and T. A. Mietzner, "Chapter 29. General Properties of Viruses," in *Jawetz, Melnick, & Adelberg's Medical Microbiology, 26e* (McGraw-Hill, 2013).
10. E. Gefroh, H. Dehghani, M. McClure, L. Connell-Crowley, and G. Vedantham, "Use of MMV as a single worst-case model virus in viral filter validation studies," PDA J. Pharm. Sci. Technol. **68**, 297–311 (2014).
11. C. Thery, M. Ostrowski, and E. Segura, "Membrane vesicles as conveyors of immune responses," Nat. Rev. Immunol. **9**, 581–593 (2009).
12. J. Zhang, S. Li, L. Li, M. Li, C. Guo, J. Yao, and S. Mi, "Exosome and exosomal MicroRNA: trafficking, sorting, and function," Genomics Proteomics Bioinf. **13**, 17–24 (2015).
13. E. van der Pol, A. G. Hoekstra, A. Sturk, C. Otto, T. G. van Leeuwen, and R. Nieuwland, "Optical and non-optical methods for detection and characterization of microparticles and exosomes," J. Thromb. Haemost. **8**, 2596–2607 (2010).
14. K. Lindfors, T. Kalkbrenner, P. Stoller, and V. Sandoghdar, "Detection and spectroscopy of gold nanoparticles using supercontinuum white light confocal microscopy," Phys. Rev. Lett. **93**, 37401 (2004).
15. F. V. Ignatovich and L. Novotny, "Real-time and background-free detection of nanoscale particles," Phys. Rev. Lett. **96**, 1–4 (2006).
16. G. G. Daaboul, A. Yurt, X. Zhang, G. M. Hwang, B. B. Goldberg, and M. S. Ünlü, "High-throughput detection and sizing of individual low-index nanoparticles and viruses for pathogen identification," Nano Lett. **10**, 4727–4731 (2010).
17. D. D. Nolte, *Optical Interferometry for Biology and Medicine* (Springer, 2012).
18. P. R. Saulson, *Fundamentals of Interferometric Gravitational Wave Detectors* (World Scientific, 1994).
19. P. A. Rosen, S. Hensley, I. R. Joughin, F. K. Li, S. N. Madsen, E. Rodriguez, and R. M. Goldstein, "Synthetic aperture radar interferometry," Proc. IEEE **88**, 333–382 (2000).
20. O. Avci, R. Adato, A. Y. Ozkumur, and M. S. Ünlü, "Physical modeling of interference enhanced imaging and characterization of single nanoparticles," Opt. Express **24**, 6094–6114 (2016).
21. R. H. Webb, "Confocal optical microscopy," Rep. Prog. Phys. **59**, 427–471 (1996).
22. S. R. P. Pavani, M. A. Thompson, J. S. Biteen, S. J. Lord, N. Liu, R. J. Twieg, R. Piestun, and W. Moerner, "Three-dimensional, single molecule fluorescence imaging beyond the diffraction limit by using a double-helix point spread function," Proc. Natl. Acad. Sci. USA **106**, 2995–2999 (2009).
23. H. Fukuda, T. Terasawa, and S. Okazaki, "Spatial filtering for depth of focus and resolution enhancement in optical lithography," J. Vac. Sci. Technol. B **9**, 3113–3116 (1991).
24. A. K.-K. Wong, *Resolution Enhancement Techniques in Optical Lithography* (SPIE, 2001).
25. K. Kamon, T. Miyamoto, Y. Myoi, H. Nagata, M. Tanaka, and K. Horie, "Photolithography system using annular illumination," Jpn. J. Appl. Phys. **30**, 3021–3029 (1991).
26. G. G. Daaboul, C. A. Lopez, J. Chinnala, B. B. Goldberg, J. H. Connor, and M. S. Ünlü, "Digital sensing and sizing of vesicular stomatitis virus pseudotypes in complex media: a model for Ebola and Marburg detection," ACS Nano **8**, 6047–6055 (2014).
27. O. Avci, N. L. Ünlü, A. Y. Ozkumur, and M. S. Ünlü, "Interferometric Reflectance Imaging Sensor (IRIS)–A platform technology for multiplexed diagnostics and digital detection," Sensors **15**, 17649–17665 (2015).
28. G. G. Daaboul, P. Gagni, L. Benussi, P. Bettotti, M. Ciani, M. Cretich, D. S. Freedman, R. Ghidoni, A. Y. Ozkumur, C. Piotto, D. Prosperi, B. Santini, M. S. Ünlü, and M. Chiari, "Digital detection of exosomes by interferometric imaging," Sci. Rep. **6**, 37246 (2016).
29. C. A. Balanis, *Antenna Theory: Analysis and Design* (Wiley-Interscience, 2005).
30. L. Novotny and B. Hecht, *Principles of Nano-Optics* (Cambridge University, 2006).
31. E. Ozkumur, J. W. Needham, D. A. Bergstein, R. Gonzalez, M. Cabodi, J. M. Gershoni, B. B. Goldberg, and M. S. Ünlü, "Label-free and dynamic detection of biomolecular interactions for high-throughput microarray applications," Proc. Natl. Acad. Sci. USA **105**, 7988–7992 (2008).
32. N. N. Boustany, S. C. Kuo, and N. V. Thakor, "Optical scatter imaging: subcellular morphometry *in situ* with Fourier filtering," Opt. Lett. **26**, 1063–1065 (2001).
33. D. W. Piston, "Choosing objective lenses: the importance of numerical aperture and magnification in digital optical microscopy," Biol. Bull. **195**, 1–4 (1998).
34. S. M. Scherr, G. G. Daaboul, J. Trueb, D. Sevenler, H. Fawcett, B. Goldberg, J. H. Connor, and M. S. Ünlü, "Real-time capture and visualization of individual viruses in complex media," ACS Nano **10**, 2827–2833 (2016).